The Covalent Binding of Splicing Inhibitors occurs via a Zinc- Assisted Enzymatic-like mechanism

Riccardo Rozza,[a] Angela Parise, [a] Jana Aupič,[a] Angelo Spinello, [b] Vlad Pena[c] and Alessandra Magistrato*[a]

[a] Dr, A., Magistrato, Dr. R.Rozza, Dr. A. Parise, and Dr. J. Aupič
CNR - Istituto Officina dei Materiali (IOM) c/o SISSA
via Bonomea 265, 34136, Trieste, Italy
E-mail: alessandra.magistrato@cnr.it

[b] Prof. A. Splinello
Department of Biological, Chemical and Pharmaceutical Sciences and Technologies
University of Palermo
90128 Palermo, Italy

[c] Prof. V. Pena
Research Group Mechanisms and Regulation of Splicing
The Institute of Cancer Research
123 Old Brompton Road, London, SW7 3RP

Abstract

Drugs modulating pre-mRNA splicing hold anticancer therapeutic potential by compensating splicing defects and rebalancing gene expression. Spliceostatins are potent antitumor agents that inhibit splicing by covalently binding to the SF3b complex via an elusive mechanism.

Here, multi-scale all-atom simulations resolved the molecular mechanism underlying the covalent linkage of spliceostatin A (SSA). We uncover that SSA binds to SF3b through a metal-assisted enzymatic-like reaction, with specific binding site residues and a zinc finger ion actively promoting the chemical process. Namely, while the zinc ion activates the Cys-S nucleophile, a flanking Lys-Asp residues pair cooperatively activates the SSA epoxy warhead, increasing its susceptibility to be attacked by Cys-S nucleophile.

A bioinformatic analysis of the Protein Data Bank revealed that zinc finger motifs flanked by nearby acidic residues are present in other spliceosome proteins, suggesting that SSA-like inhibitors could be designed for other zinc finger-containing targets. Our findings carry important implications for future drug design campaigns.

Introduction

Removal of introns and ligation of exons in pre-mRNA transcripts, i.e., pre-mRNA splicing, is an essential step of eukaryotic gene expression and diversification. [1,2] Pre-mRNA splicing leads to the formation of protein-coding mRNA or long-noncoding RNAs. Splicing is catalyzed by the spliceosome, an intricate biomolecular engine comprising hundreds of proteins and five small nuclear ribonucleoproteins (snRNPs), U1, U2, U4, U5, and U6.[3,4] The accuracy and precision with which splicing occurs are key for correct gene expression, as splicing errors can produce dysfunctional proteins or even disease states. Recognition of the reactive groups for the catalytic process is vital for splicing fidelity. [5,6] The splicesome assembles de novo at each splicing cycle and proceeds through landmark intermediate complexes (including E, A, B, C, P, and ILS). The early spliceosome complexes, E and A, are involved in recognizing and chaperoning key sequence motifs: the 5'splice site (5'SS), the branch sequence (BS), the polypyrimidine tract (PPT), and the 3'SS. Recognition of these sequences often occurs in

different ways, giving rise to alternative splicing. [7] While the 5'SS is selected by the U1 snRNP (E complex), the BS and PPT-3'SS are recognized in a cooperative manner by the SF1 protein and the U2AF heterodimer. During A complex formation, U2AF recruits U2 snRNP, which binds to the BS. The BS contains the conserved branch site adenosine (BS-A) that acts as a nucleophile of the first splicing step.[5]
The BS selection is mediated by the heptameric SF3b complex (Figure 1A), which is part of U2 snRNP, and is further composed of SF3B1, SF3B3, SF3B5 and PHF5A proteins. Among these, SF3B1 and PHF5A form a pocket that accommodates the BS-A during the selection.
Interestingly, SF3B1 and PHF5A are also upregulated in cancers.[8,9] Most notably, SF3B1 is recognized as an oncogenic driver,[10] that carries recurrent mutations in patient samples affected by different types of cancers, i.e. myelodysplastic syndrome with ringed sideroblasts, leukemia, uveal melanoma, and pancreatic cancer. These mutations induce the selection of cryptic BS and 3'SS instead of the canonical ones, leading to aberrant splicing events.[8,9,11,12]

SF3B1 is also a target of several splicing modulators that act as competitive antagonists of the BS. While SF3B1 undergoes a conformational transition from an open to closed state upon pre-mRNA binding, these splicing modulators have been shown to lock SF3B1 in the open conformation. They thus prevent BS binding [3,13–15] and trigger intron retention or exon skipping, depending on the selected competing BS sequence and the dose of the compound While some splicing modulators entered clinical trials, [16,17] their clinical potential in cancer is insufficiently explored.
Most splicing modulators targeting SF3B1 share a common central diene motif. Depending on the flanking chemical groups, they can be divided into three distinct chemotypes: herboxidiense, pladienolides, and spliceostatins (the latter belonging to the FR901464 family (Figure 1B).[11,12] All three families contain epoxy groups – highly reactive electrophiles that can interact covalently with nucleophilic groups. However, crystal structures have revealed that only spliceostatins, and the related sudemycins, can employ the epoxy group for covalent coupling. [18–22] Indeed, a recent crystal structure of two FR901464 analogs, spliceostatin A (SSA) and sudemycin 6 (Figure 1B), revealed that these modulators outcompete the BS-A and stall the spliceosome by covalently linking to a cysteine residue in one zinc finger of PFH5A. Notably, the PHF5A residue Lys29 was suggested to contribute to coupling efficacy, given its proximity to the SSA epoxide and the observed change of sensitivity to SSA in cells carrying K29A mutations.[23] Besides rationalizing the biological activity of the spliceostatin family of compounds, this finding demonstrated that splicing modulation could be achieved via covalent inhibition.
This inhibition type generally occurs through a series of discrete steps (Scheme S1): initially, the inhibitor (I) diffuses through the solution to encounter the target protein (E). Once bound, the non-covalently associated inhibitor undergoes conformational adjustments within the binding pocket (E·I) until the electrophilic warhead is optimally positioned to react with the nucleophilic residue of the target. At this stage, the chemical reaction takes place, ultimately leading to the formation of a covalent bond between the inhibitor and the biomolecule (E-I).[24]

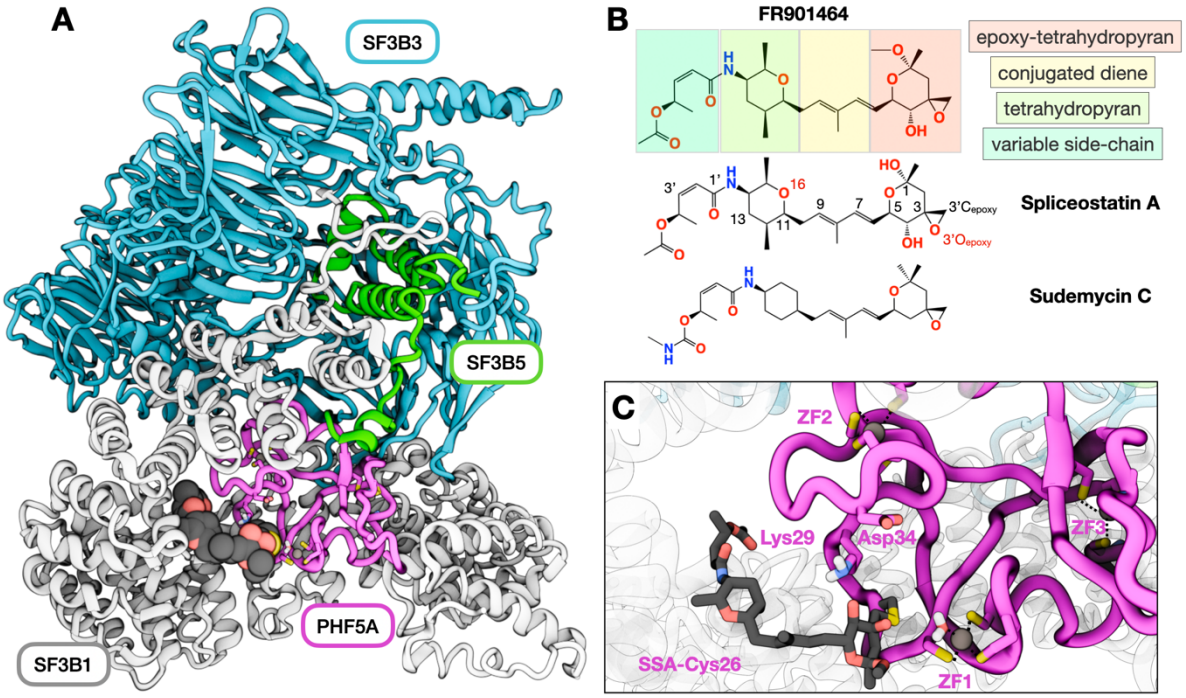

Figure 1. *– Representation of the SF3b complex and covalent inhibitors.* **A** Most representative structure extracted from the 2 µs-long Molecular Dynamics simulation trajectory of the SF3b complex (based on PDB id 7b9c) in complex with Spliceostatin A (SSA). The SSA is shown in sticks. **B** Chemical structure of FR901464 and two of its derivatives, SSA and sudemycin 6 (SD6). FR901464 is made up of four parts: (i) an epoxy-tetrahydropyran, (ii) a conjugated diene, (iii) a tetrahydropyran, and (iv) a variable side chain. **C** Close-up on the PHF5A reactive site. The three zinc fingers (ZF1, ZF2, ZF3) are shown in sticks with the carbon atoms colored according to the protein to which they belong, and the zinc atoms are represented as a grey van der Waals sphere. The Cys26-SSA residue, the other cysteine residues forming the PHF5A zinc fingers, the coordinated water molecule, and Lys29 and Asp34 are shown as sticks. Carbon atoms of SSA and PHF5A are shown in grey and pink, respectively. Oxygen, nitrogen, and sulfur are shown in red, blue, and yellow colors.

While numerous covalent inhibitors target cysteine residues and their mechanism of binding is well established, [25–27] covalent inhibitors targeting zinc-associated cysteine ligands are rare. Yet, the prevalence of zinc fingers in proteins makes this motif an attractive target for future drug design campaigns. Successful design of covalent inhibitors, however, demands a precise understanding of each step of their binding process.

Here, we performed classical and hybrid quantum-classical (QM/MM) molecular dynamics (MD) simulations to elucidate the molecular mechanisms that usher the covalent coupling of SSA to SF3b and block its restructuring for BS-A accommodation. We elucidate how SSA binds PHF5A in a reactive site of SF3b, reminiscent of an enzymatic center microenvironment. Namely, the cysteine residue responsible for the nucleophilic attack on the SSA warhead originates from and is activated by the zinc finger ion of the PHF5A protein. Additionally, the Asp34 and Lys29 pair of PHF5A residues assists the SSA covalent linkage by protonating the dissociating oxygen atom of the warhead (Figure 1C). Leveraging this mechanistic information could aid the development of novel covalent inhibitors targeting zinc finger motifs in spliceosome proteins and other biological contexts.

2 Results

2.1 Modelling the reactant E·I state

To relax the SSA/SF3b non-covalent adduct (see Supporting information for the computational details of model building and simulations protocols) and to describe the set of non-covalent interactions that SSA establishes with SF3b we perform a multi-replica 2 µs-long classical MD simulations with the FF14SB [28] AMBER force field (FF) (Figures S1-S3 and Methodology section S.21 and 2.2 of the Supporting Information). Here, the SSA sidechain and tetrahydropyran moiety (Figure 1B) hydrogen bonded with residues Arg1074 and Leu1066 from SF3B1 and formed hydrophobic interactions with Lys1067, Val1078, Val1110, Val1114, and Tyr1157 from SF3B1 and Lys25, Tyr36, and Val37 from PHF5A (Figure S3, Table S1).
Interestingly, SSA exhibited a large conformational variability when bound to SF3b. While it initially assumed a bent 'L-shape' conformation, it transited multiple times to a linear I-shaped conformation during the simulation (Figure 2A). This transition occurred upon rotation around the bond connecting the tetrahydropyran ring with the conjugated diene (dihedral angle $\omega_{O16,C11,C10,C9}$). The $\omega_{O16,C11,C10,C9}$ dihedral angle value was ~-180° and ~ -60°, for the L and I-shape states, respectively (Figure 2, S4). This rotation affected the position of the epoxy ring warhead, which lay at a distance of 22.1 and 5.9 Å from Cys26-S in the I-shape and L-shape conformations, respectively. Conversely, the SSA sidechain (Figure 1B) remained anchored to SF3B1 by hydrogen-bonding to Arg1074 and Leu106, and the SSA diene moiety was stabilized by Tyr36-PHF5A hydrophobic interaction (Figure S3). By inspecting the probability distribution of the I- and L-shape states visited during the MD simulation, we computed the free energy profile (Figure 2B) associated with the SSA conformational transition. We found that the L-shape state is the most thermodynamically favorable (ΔG= -1.9 ± 0.4 Kcal/mol) and that the free energy barrier ($\Delta G^{\ddagger}$) associated with L to I-shape interconversion is 3.1 ± 0.4 Kcal/mol. This corresponded to a conversion rate of k=1.5±1.0 $\cdot 10^{10}$ s^{-1} as estimated via the Eyring–Polanyi equation. The SF3b complex is responsible for the larger stability of the reactive L-shape SSA conformation. Indeed, metadynamics simulations (see Methodology Section S2.4) of SSA in explicit water showed that the I-shape conformation is rougthly equivalent the L-one (ΔG= 0.3±0.2 kcal/mol, Figures S5, S6) when SSA is in isolation. The interconversion of the two states exhibited a similar free energy barrier ($\Delta G^{\ddagger}$ =3.4±0.2 kcal/mol) to that computed in presence of SF3b. Quantum Mechanical (QM, DFT-B3LYP)-based calculations in implicit solvent also confirmed the trend (Figures S7).
This implies that SSA might explore distinct conformational states before anchoring to Arg1074 and Leu1066 residues and adopting a reactive conformation.

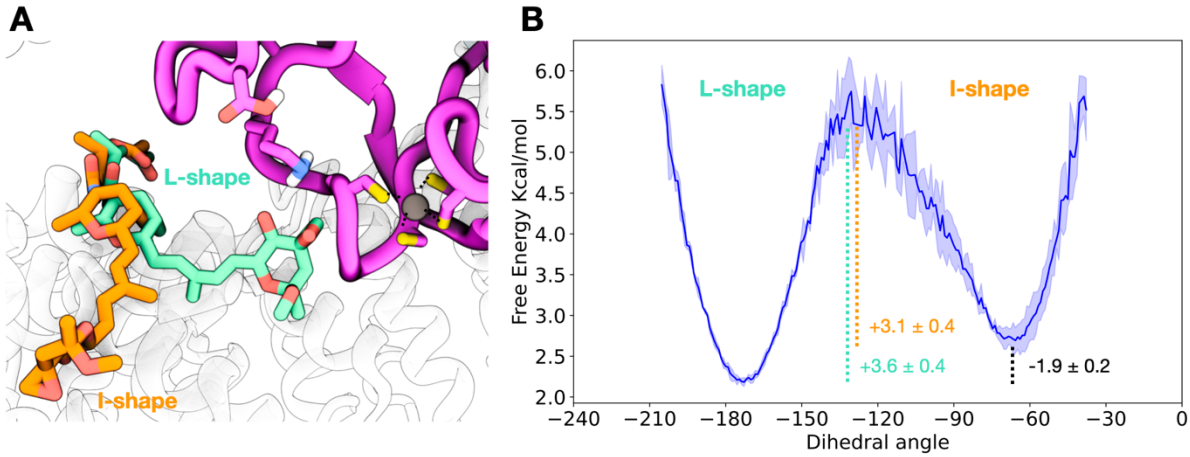

Figure 2. *Conformational Analysis of SSA.* **A** The two SSA conformations achieved by rotation along the $\omega_{O14,C9,C10,C11}$ dihedral angle of spliceostatin A are shown. The I-shape and L-shape

SSA carbon atoms are depicted in light mint and orange, respectively. **B** Free energy profile (Kcal/mol) for rotation along the SSA $\omega_{O14,C9,C10,C11}$ dihedral angle.

Next, we relaxed the reactive moieties of the E·I state, with SSA in the L-shape conformation, by performing 5.5 ps of hybrid quantum-classical (QM/MM) MD simulations using the DFT-BLYP level for the QM region, which included the reactive moieties (the reactive zinc finger, Asp34 and Lys29 residues and the reactive part of SSA (up to C10, Figure 1B) and the same FF of classical MD simulation for the MM part (see Methodology section S2.4). This method allows the description of the reactive center of a biomolecule at an accurate QM level of theory and can account for rearrangements of electronic structure and entropy changes occurring during biochemical reactions, while the rest of the system is treated with classical force fields.[29]
Although, we initially considered Lys29 and Asp34 in their ionized form based on pKa predictions (Table S1), during QM/MM MD, we observed recurrent proton transfers between them (Figure S8).

Interestingly, the Cys26 exhibited a more plastic Zn-S coordination bond than the other Zn-S bonds of the reactive zinc finger (Figure S9, S10). In particular, the S(Cys-26)-Zn bond lays for 46.6% of the time in the range from 2.45 to 2.75 Å, while the bond length of the remaining Zn-S-Cys bonds overcame the typical coordination bond length less frequently (Zn and S-Cys23, -Cys58, and -Cys6 39.8%, 30.9%, and 40.3% of the simulation time, respectively). Concomitantly, this zinc finger also deviated from the ideal tetrahedral geometry. Indeed, out of the six S-Zn-S angles, only three exhibited interquartile ranges encompassing the ideal tetrahedral value of 109.5° (Figure S11).

2.2 Covalent inhibition mechanism of spliceostatin A.
Starting from the QM/MM MD equilibrated structure of the non-covalent SSA/SF3b complex, we performed biased QM/MM MD simulations to dissect the molecular mechanism of SSA covalent binding and derive the associated Helmotz free energy profile (Figure 3) (see Methodology section S2.5).

To this end we applied the thermodynamic integration method using as reaction coordinate the distance between the epoxy carbon and oxygen atoms (3'C and 3'O, Figures 1 and S4A) of SSA (details in Methodology section S2.5) and we performed QM/MM MD simulations on RC windows ranging from 1.5 Å to 2.4 Å.
In the reactant state (RC=1.50 Å), the Cys26-S coordinated the Zn ion, and the 3'O-epoxy atom of SSA was locked into a reactive conformation by an extended interaction network involving Lys29-Nζ-PHF5A and Asp34-Oγ–H (Figure 3 and Scheme S2). Proceeding along the RC (1.60Å), the Asp34-Oγ–H proton was released to Lys29, which becomes ionized (Scheme S2,C).
At RC=1.60 Å, a water molecule approached the coordination sphere of the zinc ion, initiating Cys26-S dissociation and priming it for the nucleophilic attack on the 3'C-epoxy atom of SSA. At RC=1.65Å, the remodeling of the zinc coordination sphere was completed, with a water molecule substituting the Cys26-S ligand. At RC=1.70 Å, the 3'O-epoxy and 3'C-epoxy bond started to break due to the formation of the 3'C-epoxy and Cys26-S covalent linkage. Here, the free energy profile reaches its maximum (the transition state), corresponding to a free energy barrier of $\Delta F^{\ddagger}$= 6.9 ± 0.3 Kcal/mol (Figure 3) and a reaction rate of k=8.8±4.3 $\cdot 10^{7}$ s^{-1}, as estimated by the Eyring–Polanyi equation. At RC 1.75 Å, the 3'O-epoxy abstracted a proton from Lys29-Nζ, completing the covalent binding process. For higher RC values (2.0 – 2.4 Å), the SSA epoxy ring warhead was fully transformed into a hydroxyl group, which hydrogen

bonded to Lys29-Nζ, and the C3'-S-Cys bond between SSA and the PHF5A protein was formed (Figure 3). Overall, the nucleophilic substitution reaction between Cys26-S and the O3'-epoxy at C3' of SSA follows an SN2-type mechanism. Here, the breakage of the 3'O-epoxy and 3'C-epoxy bond is endorsed by the S-Cys nucleophilic attack and supported by the proton transfer from Lys26-Nζ (Scheme S2, Figure S12). Importantly, Asp34 orients and acidifies Lys29, thus supporting its role as a general base. This process was highly exergonic with ΔF = -59.8 ± 0.5 Kcal/mol (Supplementary movie https://doi.org/10.5281/zenodo.15308931) consistently with its irreversibility.[30]

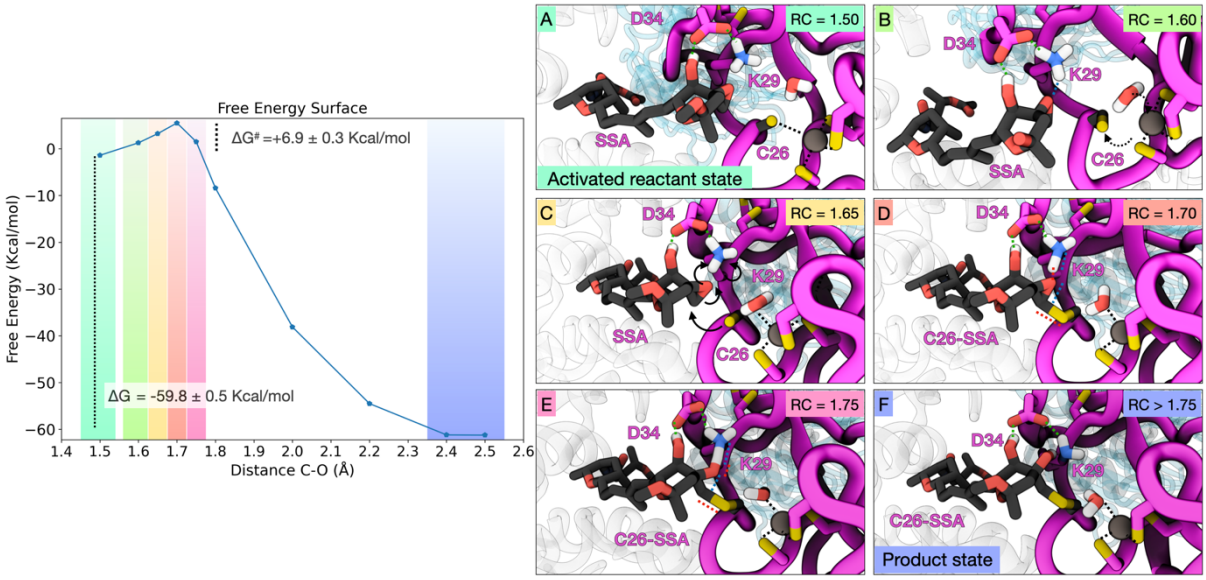

Figure3: *Reaction mechanism of SSA covalent binding to PHF5A.* Left: The Free Energy profile for SSA covalent linkage of spliceostatin A to PHF5A. Right: Series of events underlying the SSA covalent binding to PHF5A. The color assigned to each state reflects its corresponding region on the free energy profile. Green dashed lines indicate the hydrogen bond between Asp34 and Lys29. (A) (RC=1.5Å, light mint), Asp34-H protonates Lys29. (B) (R=1.60Å, lime green), a water molecule approaches the zinc coordination sphere, while the Cys26-S-Zn coordination bond starts breaking (black arrows). (C) (RC=1.65Å, pastel yellow), the water molecule substitutes the Cys26-S atom that, in turn, performs a nucleophilic attack on the C3' carbon atom of the SSA-epoxy ring (black arrows indicate the movements of the electrons). (D) and (E) (RC=1.70Å, peach pink and RC=1.75Å, light magenta) the Cys26-SSA bond is formed, while C3'-O3' epoxy bond is broken and, the SSA-O3' is protonated by Lys29. Shortening or elongating distances are shown by red and blue dashed lines, respectively. RC values in the 2.4-2.5 Å range (F, cornflower blue) correspond to the product state. Only the hydrogen atoms involved in the reaction or in the interaction with PHF5A are shown.

2.3 Modelling the product E-I state

The characterization of the product state started by performing 7 ps of QM/MM MD simulations. During this timeframe, in the zinc finger 1 with 3 Zn-Cys bonds, a water molecule remained stably coordinated to the zinc ion, completing its coordination sphere. At the same time, the SSA remained stably bound to PHF5A. The subsequent 2 µs long MD simulations of the product state revealed that SSA establishes with the SF3b complex an almost identical interaction pattern to those present in the X-ray structure (Figure S13), and the SF3b complex was characterized by a lower flexibility of the reactant state due to the lack of the covalent bond between SSA and SF3b (Figure S13-15).

3 Discussion

Small-molecule covalent drugs have several advantages in comparison to their non-covalent counterpart. Most prominently, the formation of a covalent bond between an inhibitor's reactive functional group and its target protein results in enhanced binding affinity that significantly surpasses that of non-covalent interactions alone. The covalent bond leads to an extended retention time of the inhibitor, contributing to unique pharmacodynamic characteristics that yield remarkable potency. The high efficacy of covalent inhibitors can occasionally lead to toxicity issues.[25,31,32] While first covalent drugs were discovered serendipitously and often lacked selectivity, covalent drug design has more recently yielded several successes,[24,25] sparking a renowned interest in this field. Yet, the design of efficient covalent inhibitors requires a detailed understanding of the configuration of the reactive centers and how these facilitate the reaction process. However, mechanistic information on their covalent binding is most often lacking.

Here, by performing classical and QM/MM MD simulations, we detailed the mechanism of covalent bond formation between the splicing modulator SSA and a cysteine residue of a PHF5A zinc finger. We observed that after non-covalent association, SSA established extensive interactions with the reactive center (i.e., the BP-A binding site) located at the interface of the PHF5A and SF3B1 proteins. SSA non-covalent binding mode closely resembles that of other non-covalent splicing modulators belonging to the Pladienolide and Herboxidiene families (Figure 1)[33] However, in this pocket, SSA can assume two conformations: an I-shape and a reactive L-shape, which is thermodynamically more stable, thanks to a specific set of interactions established with the binding site. In the L-shape state, the SSA epoxy moiety is optimally oriented to undergo a nucleophilic attack by one cysteine of a PHF5A zinc finger. Notably, the zinc finger ion takes an active role in this process by facilitating the conversion of the coordinated cysteine into an anionic nucleophilic thiol group. Importantly, the geometric restraints imposed by the PHF5A protein divert this zinc finger from a canonical tetrahedral geometry (Figures S10- S11). This distortion is reflected in the frequent elongation of the reactive Cys26 ligand, making it susceptible to dissociation from the zinc ion through a water-ligand exchange reaction. As such, Cys26 becomes readily available to perform a nucleophilic attack on the epoxy warhead of SSA. An electronic structure analysis of the reactive zinc finger revealed that the sulfur atom of the most frequently elongated Cys26 possesses a larger negative charge as compared to the sulfur atoms of the remaining Cysteines. This is in line with its weaker coordination to the zinc ion (Figure S17), and its enhanced nucleophilic character. Consistently with this finding, investigation of zinc-binding motifs with atomic force microscopy revealed that zinc fingers exhibiting four cysteines are characterized by high kinetic lability. [34,35] Therefore, this type of zinc finger motifs are particularly inclined towards Zn-S bond dissociation and amenable to act as nucleophilic agents (Figures S10-S11). Specifically, Cys26 is part of a zinc ribbon-type motif in which each couple of cysteine ligand are contributed by two different knuckle and lie in close proximity with a two-residue separation.[36] The tension imposed by this structural arrangement may be responsible to the enhanced flexibility and reactivity of Cys26.

In addition to the role of the zinc ions in promoting nucleophile activation, the PHF5A protein actively promotes SSA covalent binding by exposing a unique acid-base residue pair in proximity to its epoxy moiety. Reminiscent of a domino effect, the nucleophilic attack of Cys26-S on the SSA epoxy group has stemmed from the donation of a proton from Asp34 to Lys29, which subsequently releases its proton to the oxygen atom of the SSA epoxy (i.e., the leaving group in the nucleophilic substitution reaction). This facilitates the O3' epoxy dissociation from the C3' atom and its conversion into a hydroxyl group. The formation of the

covalent linkage between SSA and PHF5A is highly exoergonic (ΔF= -59.8 ± 0.5 Kcal/mol) in line with an irreversible inhibition process.
The observed mechanism, likely shared by other FR901464 family of drugs, has the chemical features of a metal-assisted enzymatic-like process: (i) the residues of the binding site specifically recognize the drug and stabilize it into a reactive (L-shape) conformation, (ii) the zinc ion assists the formation of a nucleophilic Cys moiety, (iii) the Asp34/Lys29 acid/base couple promotes the release of the leaving group. Thus, this work demonstrates that drug neighboring residues participate in endorsing the epoxy ring covalent coupling both directly – as a proton source - and indirectly by anchoring the non-reactive drug moiety. Our findings carry important implications for future drug design campaigns, suggesting that the correct positioning of the epoxy warhead relative to the zinc motif is not the only feature to consider when selecting candidates for in vitro screening. Taking into account the residues surrounding the epoxy warhead, the geometric characteristics of the zinc finger coordination sphere seem to be equally significant.
Moreover, while cysteine residues are targets of a variety of covalent drugs,[37] activation of a nucleophilic cysteine by zinc ions is rare and has been previously observed only in cysteines belonging zinc coordination sphere of the metallo-β-lactamase enzymes.[38–40]
However, zinc finger motifs are commonly found in a wide variety of proteins where they provide structural integrity and maintain functional shapes under a range of physiological conditions. Hence, owing to their abundance and biological relevance zinc fingers are a tantalizing target for covalent drug discovery efforts. To estimate the presence and the frequency of distorted $ZnCys_4$ motifs, we analyzed their characteristics in other splicing factors and splicing-related proteins as a model of the whole proteome (Figure S18, Table S3-S6). We identified several proteins containing distorted zinc finger motifs, exhibiting at least one zinc-S-Cys distance longer than 2-4-2.8 Å (Table 1). Notably, most of the identified zinc finger proteins have the same structural characteristic of the reactive zinc finger of PHF5A and showcase a ribbon-like zinc finger architecture with four ligands coming from two different knuckles and being in close proximity with an interspace of two residues [36] (Table S6). Moreover, in many of these distorted zinc finger motifs a basic residue (Lys, His, Arg) is present, and it is supported by a nearby acidic residue (Glu, His), thus resembling the acid-base pair of residues assisting the binding of SSA to SF3b **(**Table S6). This analysis suggests that, upon the binding of the appropriate inhibitor/warhead, the covalent linkage mechanism elucidated here for SSA may also be applicable to other zinc finger-containing proteins.
Nonetheless, due to their inherent kinetic lability, even canonical (undistorted) zinc finger motifs may be targeted by covalent inhibitors and therefore it may be worth considering them in drug discovery efforts.

Table 1 List of splicing-related proteins containing zinc finger motifs (first column) and their deposited PDB ID (second column)

Protein	**PDB ID**
RBM5	7PDV
RBM10	2MXV
RBM22	6ID0, 6ID1
SLU7	7W5A
ZBTB7A	7EYI

In conclusion, the zinc finger motif represents an appealing underexplored target for covalent drug discovery initiatives, and our findings collectively provide essential insights for identifying this class of novel inhibitors.

5 Acknowledgments

A. M. and R. R. thank the Italian Association for Cancer Research (AIRC) for financial support (AIRC IG 24514). AM and AP thank "Pathogen Readiness Platform for CERIC-ERIC Upgrade" – PRP@CERIC, financed under the PNRR (National Recovery and Resilience Plan) under Mission 4 "Education and Research" Component 2 "From Research to Enterprise", Investment Line 3.1 "Fund for the creation of an integrated system of research and innovation infrastructures", funded by the European Union – Next Generation EU. A.M. and J.A. thanks the PNRR: National Center for Gene Therapy and Drugs based on RNA Technology CUP B83C22002860006 CN_0000004.
The authors thank CINECA, the Italian super-computing center, for computational resources via the "IsB27_EDR" and "IsCc6_SF3bMod" projects.

Supporting Information

Supplementary data consist of Scheme S1-S2, Supplementary Tables S1-S6, Supplementary Figures S1-S19, and Supplementary Movie 1 (https://doi.org/10.5281/zenodo.15308931).

[1] M. E. Rogalska, C. Vivori, J. Valcárcel, *Nat Rev Genet* **2023**, *24*, 251–269.
[2] J. Tholen, W. P. Galej, *Current Opinion in Structural Biology* **2022**, *77*, 102461.
[3] S. Rinaldi, E. Moroni, R. Rozza, A. Magistrato, *J. Chem. Theory Comput.* **2024**, *20*, 993–1018.
[4] J. Borišek, L. Casalino, A. Saltalamacchia, S. G. Mays, L. Malcovati, A. Magistrato, *Acc. Chem. Res.* **2021**, *54*, 144–154.
[5] J. Aupič, J. Borišek, S. M. Fica, W. P. Galej, A. Magistrato, *Nat Commun* **2023**, *14*, 8482.
[6] J. Borišek, A. Magistrato, *ACS Catal.* **2020**, *10*, 5328–5334.
[7] J. Borišek, A. Saltalamacchia, A. Gallì, G. Palermo, E. Molteni, L. Malcovati, A. Magistrato, *Biomolecules* **2019**, *9*, 633.
[8] C. Sun, *Cell. Mol. Life Sci.* **2020**, *77*, 3583–3595.
[9] Y.-Z. Zheng, M.-Z. Xue, H.-J. Shen, X.-G. Li, D. Ma, Y. Gong, Y.-R. Liu, F. Qiao, H.-Y. Xie, B. Lian, W.-L. Sun, H.-Y. Zhao, L. Yao, W.-J. Zuo, D.-Q. Li, P. Wang, X. Hu, Z.-M. Shao, *Cancer Research* **2018**, *78*, 3190–3206.
[10] C. J. David, J. L. Manley, *Genes Dev.* **2010**, *24*, 2343–2364.
[11] A. K. Ghosh, J. L. Mishevich, M. S. Jurica, *J. Nat. Prod.* **2021**, *84*, 1681–1706.
[12] K. A. Effenberger, V. K. Urabe, M. S. Jurica, *WIREs RNA* **2017**, *8*, e1381.
[13] R. Rozza, P. Janoš, A. Spinello, A. Magistrato, *Expert Opinion on Drug Discovery* **2022**, *17*, 1095–1109.
[14] C. Cretu, A. A. Agrawal, A. Cook, C. L. Will, P. Fekkes, P. G. Smith, R. Lührmann, N. Larsen, S. Buonamici, V. Pena, *Molecular Cell* **2018**, *70*, 265-273.e8.
[15] D. Inoue, O. Abdel-Wahab, *Cancer Cell* **2016**, *30*, 371–373.
[16] D. P. Steensma, M. Wermke, V. M. Klimek, P. L. Greenberg, P. Font, R. S. Komrokji, J. Yang, A. M. Brunner, H. E. Carraway, L. Ades, A. Al-Kali, J. M. Alonso Dominguez,

A. Alonso, C. C. Coombs, H. J. Deeg, W. B. Donnellan, J. M. Foran, G. Garcia-Manero, M. B. Maris, M. McMasters, J.-B. Micol, J. Perez De Oteyza, F. Thol, E. S. Wang, J. M. Watts, S. Buonamici, A. Kim, V. Gourineni, A. J. Marino, N. Rioux, J. Schindler, S. Smith, H. Yao, X. Yuan, K. Yu, U. Platzbecker, *Blood* **2019**, *134*, 673–673.

[17] Hemavant Sciences GmbH, *An Open-Label, Multicenter Phase 1 Trial to Evaluate the Safety, Pharmacokinetics and Pharmacodynamics of Splicing Modulator H3B-8800 for Subjects With Myelodysplastic Syndromes, Acute Myeloid Leukemia, and Chronic Myelomonocytic Leukemia*, Clinicaltrials.Gov, **2024**.

[18] H. Nakajima, Y. Hori, H. Terano, M. Okuhara, T. Manda, S. Matsumoto, K. Shimomura, *J. Antibiot.* **1996**, *49*, 1204–1211.

[19] C. F. Thompson, T. F. Jamison, E. N. Jacobsen, *J. Am. Chem. Soc.* **2021**, *123*, 9974–9983.

[20] S. Osman, B. J. Albert, Y. Wang, M. Li, N. L. Czaicki, K. Koide, *Chemistry – A European Journal* **2011**, *17*, 895–904.

[21] K. C. Nicolaou, D. Rhoades, S. M. Kumar, *J. Am. Chem. Soc.* **2018**, *140*, 8303–8320.

[22] Y. Yoshikawa, A. Ishibashi, T. Takehara, T. Suzuki, K. Murai, Y. Kaneda, K. Nimura, M. Arisawa, *ACS Med. Chem. Lett.* **2020**, *11*, 1310–1315.

[23] C. Cretu, P. Gee, X. Liu, A. Agrawal, T.-V. Nguyen, A. K. Ghosh, A. Cook, M. Jurica, N. A. Larsen, V. Pena, *Nat Commun* **2021**, *12*, 4491.

[24] A. Parise, I. Romeo, N. Russo, T. Marino, *International Journal of Molecular Sciences* **2021**, *22*, 9792.

[25] L. Boike, N. J. Henning, D. K. Nomura, *Nat Rev Drug Discov* **2022**, *21*, 881–898.

[26] C. Borsari, E. Keles, J. A. McPhail, A. Schaefer, R. Sriramaratnam, W. Goch, T. Schaefer, M. De Pascale, W. Bal, M. Gstaiger, J. E. Burke, M. P. Wymann, *J. Am. Chem. Soc.* **2022**, *144*, 6326–6342.

[27] X. Lu, J. B. Smaill, A. V. Patterson, K. Ding, *J. Med. Chem.* **2022**, *65*, 58–83.

[28] J. A. Maier, C. Martinez, K. Kasavajhala, L. Wickstrom, K. E. Hauser, C. Simmerling, *J. Chem. Theory Comput.* **2015**, *11*, 3696–3713.

[29] P. Janoš, A. Spinello, A. Magistrato, *Current Opinion in Chemical Biology* **2021**, *61*, 1–8.

[30] M. S. Cohen, C. Zhang, K. M. Shokat, J. Taunton, *Science* **2005**, *308*, 1318–1321.

[31] L. Huang, Z. Guo, F. Wang, L. Fu, *Sig Transduct Target Ther* **2021**, *6*, 1–20.

[32] C.-T. Yeh, T.-T. Chen, P. B. Satriyo, C.-H. Wang, A. T. H. Wu, T.-Y. Chao, K.-Y. Lee, M. Hsiao, L.-S. Wang, K.-T. Kuo, *Oncogenesis* **2021**, *10*, 1–13.

[33] J. Borišek, A. Saltalamacchia, A. Spinello, A. Magistrato, *J. Chem. Inf. Model.* **2020**, *60*, 2510–2521.

[34] D. Picot, G. Ohanessian, G. Frison, *Chemistry – An Asian Journal* **2010**, *5*, 1445–1454.

[35] J. Perales-Calvo, A. Lezamiz, S. Garcia-Manyes, *J. Phys. Chem. Lett.* **2015**, *6*, 3335–3340.

[36] S. S. Krishna, I. Majumdar, N. V. Grishin, *Nucleic Acids Research* **2003**, *31*, 532–550.

[37] S. Ray, A. S. Murkin, *Biochemistry* **2019**, *58*, 5234–5244.

[38] P.-W. Kang, J.-P. Su, L.-Y. Sun, H. Gao, K.-W. Yang, *European Journal of Pharmaceutical Sciences* **2020**, *142*, 105161.

[39] J. Chiou, S. Wan, K.-F. Chan, P.-K. So, D. He, E. W. Chan, T. Chan, K. Wong, J. Tao, S. Chen, *Chem. Commun.* **2015**, *51*, 9543–9546.

[40] G. Ciardullo, M. Prejanò, A. Parise, N. Russo, T. Marino, *J. Chem. Theory Comput.* **2025**, *21*, 1422–1431.
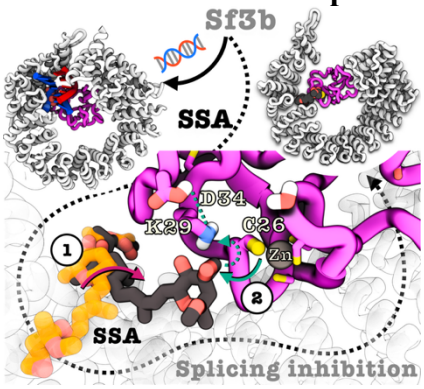
Table of Contents Graphics